Supervised Learning based Multimodal MRI Brain Tumour Segmentation using Texture Features from Supervoxels

Mohammadreza Soltaninejad [a], Guang Yang [b,c], Tryphon Lambrou [a], Nigel Allinson [a], Timothy L Jones [d], Thomas R Barrick [e], Franklyn A Howe [e], Xujiong Ye [a*]

Affiliations:

[a] School of Computer Science, University of Lincoln, Lincoln, LN6 7TS, UK (emails: {msoltaninejad | tlambrou | nallinson | xye}@lincoln.ac.uk)

[b] National Heart and Lung Institute, Imperial College London, London, SW7 2AZ, UK (g.yang@imperial.ac.uk)

[c] Neurosciences Research Centre, Molecular and Clinical Sciences Institute, St. George's, University of London, London, SW17 0RE, U.K.

[d] Academic Neurosurgery Unit, St. George's, University of London, London, SW17 0RE, UK (timothy.jones@stgeorges.nhs.uk);

[e] Neurosciences Research Centre, Molecular and Clinical Sciences Institute, St. George's, University of London, London, SW17 0RE, U.K. (emails: {tbarrick | howefa} @sgul.ac.uk).

***Corresponding Author:** Xujiong Ye

School of Computer Science, University of Lincoln, Lincoln, LN6 7TS, UK

Email: xye@lincoln.ac.uk , Tel: +44 (0) 1522 837344

Funding: This research was supported by European FP7 collaborative Project "MyHealthAvatar" (600929). MRI data were obtained during the EU FP7 "eTUMOUR" project (LSHC-CT-2004-503094).

Abstract

Background: Accurate segmentation of brain tumour in magnetic resonance images (MRI) is a difficult task due to various tumour types. Using information and features from multimodal MRI including structural MRI and isotropic (p) and anisotropic (q) components derived from the diffusion tensor imaging (DTI) may result in a more accurate analysis of brain images.

Methods: We propose a novel 3D supervoxel based learning method for segmentation of tumour in multimodal MRI brain images (conventional MRI and DTI). Supervoxels are generated using the information across the multimodal MRI dataset. For each supervoxel, a variety of features including histograms of texton descriptor, calculated using a set of Gabor filters with different sizes and orientations, and first order intensity statistical features are extracted. Those features are fed into a random forests (RF) classifier to classify each supervoxel into tumour core, oedema or healthy brain tissue.

Results: The method is evaluated on two datasets: 1) Our clinical dataset: 11 multimodal images of patients and 2) BRATS 2013 clinical dataset: 30 multimodal images. For our clinical dataset, the average detection sensitivity of tumour (including tumour core and oedema) using multimodal MRI is 86% with balanced error rate (BER) 7%; while the Dice score for automatic tumour segmentation against ground truth is 0.84. The corresponding results of the BRATS 2013 dataset are 96%, 2% and 0.89, respectively.

Conclusion: The method demonstrates promising results in the segmentation of brain tumour. Adding features from multimodal MRI images can largely increase the segmentation accuracy. The method provides a close match to expert delineation across all tumour grades, leading to a faster and more reproducible method of brain tumour detection and delineation to aid patient management.

Keywords: Brain tumour segmentation, Diffusion tensor imaging, Multimodal MRI, Random forests, Supervoxel, Textons

1. Introduction

Brain tumours can arise from abnormal growth of the cells inside the brain or can develop from cells that have spread to the brain from a cancer elsewhere. There are a wide variety of brain tumour types that are classified according to their cell of origin, and can be categorised as low or high grade depending on their malignancy and growth characteristics. Diagnosis of tumour grade and type is essential for optimum treatment. Medical imaging modalities are used for detection and assessment of tumours. Among these medical imaging modalities, magnetic resonance imaging (MRI) is the most widely used for clinical diagnosis, treatment selection, prognosis and to aid surgery and radiotherapy planning [1]. Due to the multimodal nature of MRI there are a range of image types and contrasts that enable a subtle radiological assessment of tumour type.

Computer-aided procedures are being developed to aid conventional neuroradiological diagnosis and treatment planning. Image processing with pattern recognition and machine learning algorithms are widely used for analysis as an aid to interpretation of medical images. Segmentation techniques have been proposed for several clinical applications [2]. For brain tumours, image segmentation may aid the fast and objective measurement of tumour volume and also find patient-specific features that aid diagnosis and treatment planning [3].

A primary segmentation task in the case of brain tumours is to accurately label the tumour tissue and the normal brain regions. In many cases, the tumour region is visually distinct, but it is a challenge for accurate and reproducible segmentation and characterisation of the abnormality that works across multiple tumour types and with

different MR scanner types [3]. Even within one pathological class of tumour there is a large variety and complexity of tumour imaging characteristics such as signal intensity, image texture, and its size, shape, location with respect to other normal brain structures. Some tumours with high grades are quite heterogeneous having a necrotic core surrounded by viable tumour that infiltrates into the normal brain tissue. Adjacent non-tumour regions may also look abnormal due to an inflammatory response creating areas of oedema. Hence it is a difficult task to develop a universal method to segment tumours accurately [4]. Clinical needs for tumour segmentation include dose-planning for radiotherapy, assessing changes in tumour volume when monitoring low to high grade transformation of glial tumours, and monitoring the response to treatment.

Manual segmentation of tumours in MRI images is time-consuming and subjective since it is dependent on the operators' skill and experience, hence inter-operator reproducibility can be low. Automatic computer assisted procedures have the potential to provide more objective segmentation of tumours, and also allow large-scale multimodal MRI data to be analysed within a reasonable processing time. Nevertheless, manual segmentation by experts is commonly used as a gold standard for assessing the automatic or computer-aided segmentation techniques and also for training the systems.

1.1. Related Works

The research work for automatic brain tumour segmentation has increased in recent decades which represents the demand for this area of research and currently it is still in progress [5]. Several methods have been proposed in the literature for detection and segmentation of tumours in MR images [6]. The segmentation methods can be categorized into

unsupervised and supervised learning based methods [3].

Unsupervised segmentation techniques use clustering methods for segmenting unlabelled images. Expectation maximization (EM) is one of the popular unsupervised methods which was utilized in [7] with the application on multimodal conventional MRI (C-MRI) data in which the prior-knowledge of the normal brain was obtained from atlas of normal brain and the intensity model for tumour was estimated. Another popular unsupervised clustering method is fuzzy *c-Means* (FCM) and in [8] an improved approach was proposed for brain tumour segmentation which included the information from class centres to regularize the clusters. A nonparametric model-based method was proposed in [9]. The method was based on graph-cut distribution without involving the training procedure and has low computation time. A comparison of most recent unsupervised methods for brain tumour segmentation was presented in [10]. They also introduced an unsupervised method for segmentation of high grade gliomas (HGG). Their method was applied to multiparametric MRI data which conventional T2-weighted and contrast enhanced MRI were combined with other modalities including diffusion-weighted imaging (DWI). DWI is considered in our paper, but using parameters derived from diffusion tensor imaging (DTI). The advantage of unsupervised methods is that they do not require a large amount of training data. However, the methods are not able to automatically label segmentation results to different tissue types (e.g. tumour core, oedema, necrosis, or healthy brain tissue). Those tissue types are determined by users, which makes the methods inherently semi-automated. Furthermore, using unsupervised segmentation for brain tumours is challenging due to the lack of shape or intensity prior [3].

Supervised learning based algorithms use training data for segmentation of tumours,

which are labelled by experts. Helen *et al.* developed a hybrid method for brain tumour segmentation based on clustering, classification and conventional segmentation methods [11]. Several works applied random forests (RF) classification and its variants to segment tumours [12–15]. In [12] several features including intensity, geometry and asymmetry from multiple modalities are applied to a random forests classifier. Extremely randomized trees were used in [13] with high level features including appearance and context-based features calculated from nonlinear transformation of the images. The work in [14] used Gaussian mixture models for different individual protocols (modalities) (i.e. T1-weighted, T2-weighted and FLAIR) separately. Goetz *et al.* [15] proposed a new random forest based method which uses domain adaptation to reduce sample selection errors. Bauer *et al.* [16] proposed using RF and conditional random fields (CRF). They suggested using the probabilistic output of the RF to control the spatial regularisation of CRF. Several feature sets, including first order and symmetry features, were extracted from fixed sized local patches. Geremia *et al.* [17] proposed spatially adaptive RF, which performed a hierarchical segmentation from coarse to fine segmentation. Tustison *et al.* [12] proposed using morphological and contextual features to better discriminate the homogeneity of the tumour. They also suggested using MRF to encourage the spatial regularisation. Festa *et al.* [18] used RF with different image features which were voxel based. Their RF parameters included 50 number of trees and tree depth of 25. The method was test on the Multimodal Brain Tumor Image Segmentation Benchmark (BRATS) 2013 dataset [24,25]. The RF parameters were set using leave-one-out cross-validation of the training dataset. The training data points were downsampled and divided to half for normal brain tissue and half for tumour and oedema to make the data balanced for more accurate classification.

Lefkovits *et al.* [19] optimised RF for brain tumour segmentation in MRI for the BRATS dataset.

Deep learning, as one of the advanced supervised techniques, has recently been widely used to help identify, classify, and quantify patterns in medical images. A fully automatic brain tumour segmentation based on deep neural networks (DNNs) architecture was presented in [43]. The method exploited both local details and global contextual features simultaneously. To overcome the computational burden of processing 3D medical scans, a dual pathway, 11-layers deep, three-dimensional Convolutional Neural Network (CNN) was presented in [44]. The method incorporates both local and larger contextual information and processes the input MRI images at multiple scales simultaneously. A 3D fully connected CRF is then used to removes false positives for accurate brain tumour segmentation. Very recently, Zhao et al. [45] integrated fully convolutional neural network (FCNNs) and CRFs in a unified framework for brain tumour segmentation with appearance and spatial consistency.

Few studies have combined different MRI modalities for brain tumour segmentation. A number of advanced algorithms [18,20–23] were presented in [5] using the MICCAI BRATS dataset [24, 25]. The methods were based on segmentation of different tumour tissues, i.e. tumour core, oedema, necrosis, using multimodal conventional MRI containing FLAIR, T1-weighted, T1-contrast and T2 protocols [26]. In [27] C-MRI and DTI were combined and fed to support vector machines (SVM) to segment different tumour tissue types. In another work [23], which used decision forests to segment HGG, the segmentation results by adding DTI were improved compared to using only C-MRI modalities. Combination of DWI with C-MRI has been also researched for unsupervised

methods such as spatial fuzzy *c-Means* [28] to improve the segmentation results. The BRATS dataset [24,25] included C-MRI modalities, whereas our own clinical dataset contains both C-MRI and DTI modalities. In this paper, we have combined multimodal MRI for accurate segmentation and labelling of different tumour parts (e.g. tumour core and oedema).

Most previous studies are voxel-wise, in which a window or subarea around a voxel is normally used to extract features for labelling (classifying) the voxel. In the case of multimodal MRI data, it is comprised of millions of voxels (i.e. the sum of all voxels across each image modality) and consequently voxel based methods usually require significant computational time. Few studies have used superpixel or supervoxel methods for segmentation. Wu *et al.* used supervoxel based features in a conditional random fields (CRF) framework to detect brain tumours [29]. In [21] Markov random fields are applied on supervoxels of the images to segment the tumours based on intensity probabilities.

In this paper, we aim to segment brain tumour parts (core and oedema) using a novel multimodal MRI supervoxel based method (combining DTI with conventional MRI modalities). Gabor texton based features; alongside first order intensity based statistical features are calculated for each supervoxel and used in a random forest classifier to label supervoxels into different tissue types.

1.2. Our Contribution

Most of the existing studies on brain tumour segmentation are performed on conventional MRI protocols (i.e. FLAIR, T1-weighted (with contrast) and T2-weighted), which are

based on qualitative image intensities. In this study, in addition to the conventional MRI sequences, we also consider the isotropic (p) and anisotropic (q) diffusion components derived from DTI [30], which provides parameters that relate to the average microscopic movement of water within tissue structure (p) and whether this movement has an anisotropic element of diffusion (q) such as for the water in white matter fibers. We hypothesize that combining DTI and C-MRI may provide quantitative features that increase the classification accuracy and improve tumour segmentation results.

Instead of applying voxel based techniques commonly used in classification-based segmentation of brain tumour in MR images, in this paper, a supervoxel based method is considered, which partitions an image into a number of small 3D patch volumes. The advantage of the supervoxel based method is that the required computation for classification in the new feature space can be significantly reduced. Feature vector size in the general case of supervoxels is less than those that are based on image voxels (i.e. moving window).

The main contributions of our method can be summarised as follows:

- The supervoxel is formed using multimodal MRI, including FLAIR, T1-weighted (with contrast), T2-weighted, p and q diffusion maps. Unlike existing methods [31] in which a supervoxel is calculated from one single MRI protocol, in this paper, information from multimodal images is combined to produce supervoxel boundaries across multiple image protocols.
- A unified framework is built to classify each supervoxel using features calculated from multimodal MRI for segmentation of brain tumour.

- We have shown that our novel histogram of texton descriptors, calculated using a set of Gabor filters with different sizes and orientations provide improved performance for classification of brain tumour supervoxels. Since supervoxels are limited to clusters of similar intensities within each MRI modality, using the distribution of local textures inside each supervoxel improves further classification of supervoxels, Texton has demonstrated its advantages of providing significant information to distinguish various patterns.

The paper is organised as follows. Section II describes the proposed method, which consists of supervoxel segmentation, feature extraction, classification, and final segmentation. Section III presents experimental results and is followed by the discussion in Section IV and Section V.

2. Materials and Methods

2.1. Data Acquisition

Brain tumour patient data was acquired using a GE Signa Horizon LX 1.5T MRI system (GE Healthcare, Milwaukee, WI, USA) equipped with a maximum field gradient strength of 22mT/m and using a quadrature head coil. The multimodal MRI acquisition used in this study is described below.

FLAIR and T1-weighted images were acquired in the axial plane with a field of view (FOV) 240 x 240 mm^2, matrix size 256 x 256 and 5 mm slice thickness for FLAIR and 2.8 mm for T1 with no slice gap. The following acquisition parameters were used for FLAIR (TE = 133 ms, TR = 9000 ms, inversion time 2200 ms, band width = 61.04 Hz) and

T1 weighted (TE = 14 ms, TR = 600 ms, band width = 122.1 Hz). T1-weighted images were acquired both with and without intravenously administered contrast agent (0.1 mmol/kg gadoterate meglumine, Dotarem).

T2-weighted images were acquired in the axial plane using a dual echo sequence with TR = 3500 ms and TE=14/98 ms and FOV of either 220 x 220 mm^2 or 240 x 240 mm^2, a 256 x 256 acquisition matrix, and 29 slices with 5 mm thickness [32].

DTI data were acquired using a diffusion-weighted spin-echo echo-planar imaging sequence. A b_0 acquisition was made without diffusion gradients (b=0 s/mm^2) and diffusion weighted images were acquired using b=1000 s/mm^2 with 12 gradient directions [33]. The FOV was 240 x 240 mm^2 with a 96 x 96 acquisition matrix. In total 50 contiguous slices (2.5 mm in-plane resolution) were acquired with a slice thickness of 2.8 mm. TR and TE were 8 secs and 88 ms, respectively. The data was interpolated to a 256 x 256 matrix. The diffusion parameters p and q for isotropic and anisotropic diffusion respectively were calculated as proposed by Peña *et al.* [30].

A cohort consisting of 11 brain tumour patients (2 grade III, and 9 grade IV) retrospectively entered the study and were scanned using the multimodal MRI protocol. Histological diagnosis was available for all tumours. Patient ages at the time of scanning ranged from 33 to 73 years (mean age 53 and standard deviation 7). The ground truths (GT) were provided by a senior and experienced consultant neurosurgeon. The annotation protocol and the corresponding GT labels are as follows

1- Oedema; the boundaries are drawn using the FLAIR images,

2- Tumour core; the boundaries are drawn using T1-contrast images,

0- Others (including healthy brain tissues and background).

2.2.Overview of the Method

Our method is comprised of four steps (preprocessing, supervoxel partitioning, feature extraction and classification) that are depicted in Fig 1 and described below.

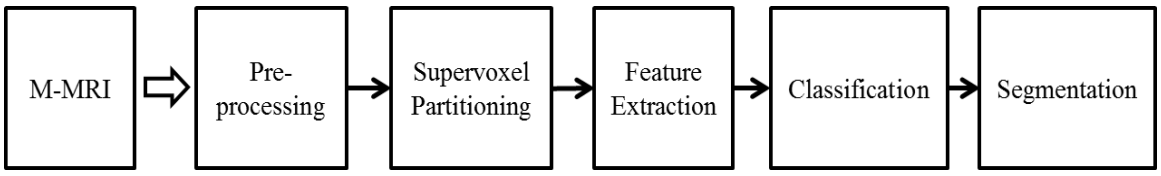

Fig. 1. Flowchart of the proposed multimodal MRI segmentation method for segmentation of brain tumour.

After image preprocessing, the supervoxel segmentation partitions the MRI data into equally sized patches with similar intensity ranges. Supervoxels are calculated based on a distance matrix which is formed using a combination of multimodal images. Use of different MRI modalities can enhance the supervoxel segmentation by identifying image boundaries simultaneously across all available images. For each supervoxel patch, a number of features including statistical and texture features are calculated. The supervoxels are classified into tumour core, oedema, and others (i.e. normal brain tissues and background) using a random forests classifier. The supervoxels of tumour core and oedema are then grouped together to obtain the corresponding tumour boundaries.

2.3.Preprocessing

DTI data were realigned to remove eddy current distortions using eddy correct (FSL Software Library by FMRIB [34]) prior to generating p and q maps. Images were skull stripped using Brain Extraction Tool in FSL. All conventional MRI data were then co-registered to the DTI b_0 data using an affine transformation with a mutual information based cost function using Statistical Parametric Mapping (SPM12 [35]) to avoid interpolation of quantitative diffusion characteristics.

The image intensities are normalised with a two-step procedure: histogram matching and dynamic range normalisation. First, one case (one patient data) is selected as reference and the histogram of each image protocol of other cases are matched to the corresponding protocol of the reference case (left and right pipelines in Fig. 2). To eliminate the bias of the matched histogram to the reference case, another block ("Histogram Matching 2" in Fig. 2) is added to the process according to [36]. The average of all the new histograms including the initial reference case is calculated for each protocol and the histograms are again matched to the new reference, e.g. the average histogram for each protocol. In the second stage, for each case, the intensity of new images of all the protocols obtained from the first step are linearly normalized to the dynamic range of the corresponding FLAIR related to that case. This is to ensure that, in the feature extraction stage, for each patient case, images from different protocols have similar intensity dynamic ranges.

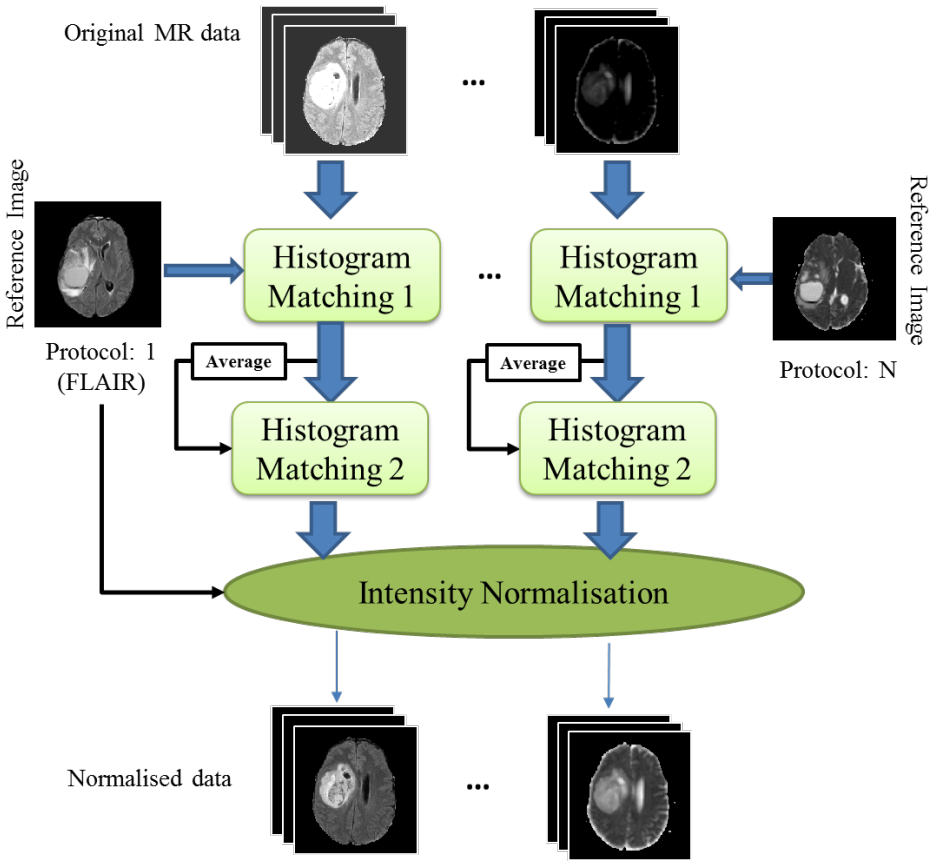

Fig. 2. Flowchart of the multimodal normalisation and histogram matching of the MR dataset.

2.4. Partitioning MR Volumes to Supervoxels

Most of voxel-wise classification algorithms used fixed 3D patches (Fig. 3(a)). For example, Festa *et al.* [18] used 3D cube of different sizes which is centred in each voxel for feature extraction and then assigned the features to that voxel. Instead of fixed 3D cube volume, supervoxel is used as the patch for feature extraction. Supervoxel includes voxels with similar characteristics (e.g. intensity, red points inside the volume shown in Fig.3(b)), while 3D cubic patch is fixed and include voxels which are within the patch volume regardless of their values and their relevance to adjacent voxels (blue points inside the

volume shown in Fig.3(a)).

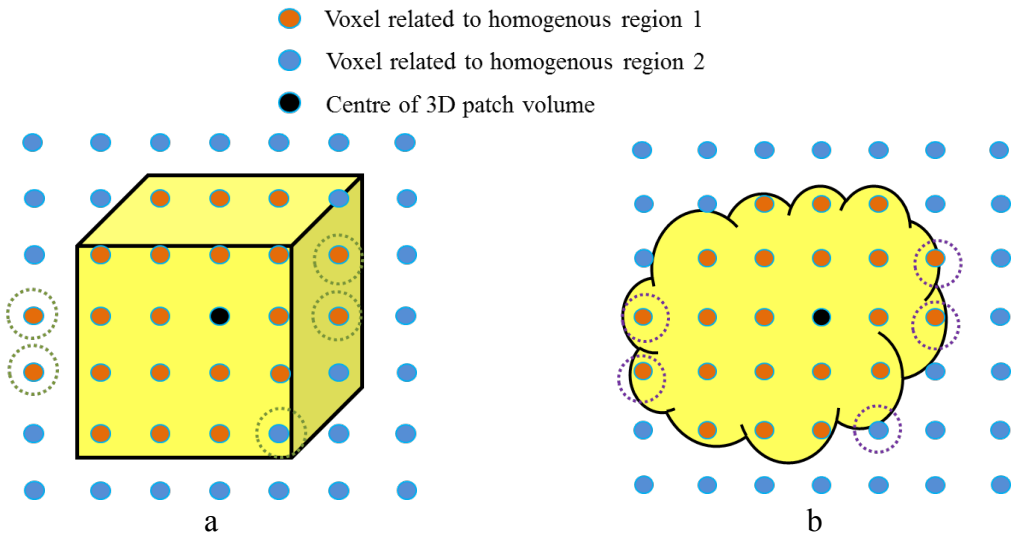

Fig. 3. Fixed and flexible 3D volumes for feature extraction. a) fixed size cubic patch. b) flexible homogenous patch volume.

The aim of supervoxel clustering is to group an image into a predefined number of portions, which have similar intensity range. In this paper, the simple linear iterative clustering (SLIC) superpixel method [37] is extended to extract 3D supervoxels for the segmentation of brain tumour. A brief description of SLIC is given below.

In our method, the initial grid height is chosen based on the slice thickness (spatial resolution in Z direction) of the MRI images and the spatial resolution ratio (R_s) between X and Y directions (i.e. R_x and R_y). Therefore, R_s is obtained using

$$R_S = \frac{R_x}{R_y}. \quad (1)$$

For our own clinical dataset, the resolutions in X and Y directions are the same (so R_s=1). Since all the data are co-registered in the preprocessing stage, the slice thickness for each

dataset is consistent through all the slices in each image data set which is considered as R_t. It should be noted that registration of the data is very important to perform this multimodal supervoxel segmentation. If the supervoxel width is considered to be W_S voxels, its height, H_S is calculated from the ratio of slice spatial resolution to slice thickness

$$H_S = \left\| W_S \times \frac{R_S}{R_t} \right\|. \quad (2)$$

The operator ||…|| means the nearest rounding integer to the value. The minimum value for supervoxel height, H_S, is considered to be 3, whilst, H_S=1 results in 2D segments which are considered as superpixels. Fig.4 presents a schematic illustration of calculating the initial supervoxel parameters from the MR input data considering the voxel resolutions.

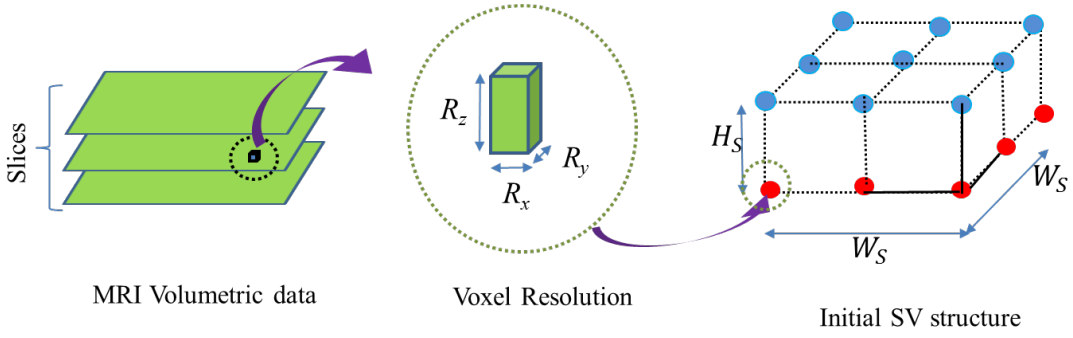

Fig. 4. Initial supervoxel structure calculation based on MR voxel resolution parameters. Ws and Hs represent initial supervoxel width and height. Rx and Ry relate to spatial resolution of the voxel in XY plane, and Rz relates to slice thickness.

In the first instance, the geometrical centres of the initial grids are considered as supervoxel region centres. The mean value of the voxel coordinates inside the supervoxel provides the centre of gravity of that supervoxel. The locations of the centres of gravity are updated during each iteration. The distance between each voxel in the dataset to the bounded cluster centres are calculated and then a label of the closest cluster centre is assigned to that target voxel. The final distance is comprised of both intensity and location

distances. The intensity distance, d_c, is calculated by defining the intensity difference between the *i*th and the *j*th voxel according to the following formula:

$$d_c = \sqrt{(I_j - I_i)^2}, \tag{3}$$

where, I_i and I_j are the normalized intensity values of the *i*th and the *j*th voxel, respectively. The location distance, d_s, between the two voxels is calculated as follows,

$$d_s = \sqrt{(R_x(x_j - x_i))^2 + (R_y(y_j - y_i))^2 + (R_z(z_j - z_i))^2}, \tag{4}$$

where, (x_i, y_i, z_i) is the coordinate of voxel *i* and R_x, R_y and R_z are the voxel resolutions.

The distance measure [37] is then defined as,

$$D = \sqrt{d_c^2 + \left(\frac{d_s}{w_s}\right)^2 m^2}, \tag{5}$$

where, m, is the compactness coefficient. A higher value of m results in more compact segments and a lower value creates more flexible boundaries.

Fig.5 shows the supervoxel segmentation of a brain tumour using MRI FLAIR with two different initial grid sizes.

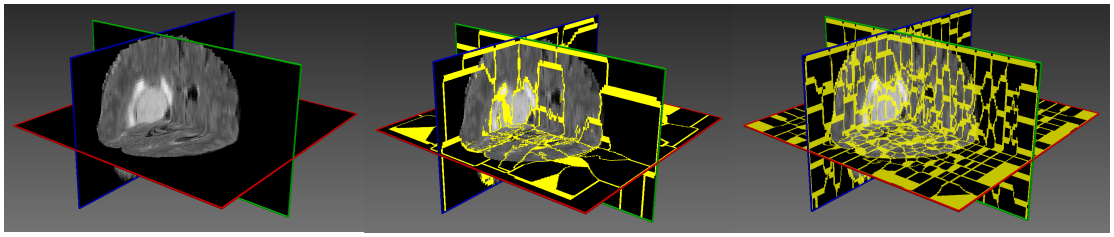

(a) (b) (c)

Fig. 5. Supervoxel segmentation of MRI FLAIR for different supervoxel sizes: a) original image, b) large supervoxel size (30 × 30 × 11), c) small supervoxel size (15 × 15 × 5).

Supervoxel segmentation of multimodal MRI data is not straightforward as tissue boundaries apparent on one MRI protocol, for example, on T1-weighted (with contrast) are not necessarily apparent on other MRI protocols such as DTI or FLAIR, and vice versa. Hence supervoxel boundaries determined independently from each MRI protocol will not match, creating tissue partial volume effects at supervoxel boundaries. To solve this problem, we adapt the supervoxel intensity distance equation (3) in a multidimensional formation and apply this across all MRI protocols, to determine a multimodal supervoxel cluster. Assuming that the multimodal MRI data is acquired with MRI protocols P_1, P_2, …, P_N, giving the images $\{I_{P1}, I_{P2}, \ldots, I_{PN}\}$ then the distance equation for multimodal MRI data is,

$$d_c = \sqrt{\left(I_{Voxel,P_1} - I_{Center,P_1}\right)^2 + \cdots + \left(I_{Voxel,P_N} - I_{Center,P_N}\right)^2}, \tag{6}$$

where, $I_{Voxel,Pi}$ is the grey-level intensity corresponding to the *voxel* in protocol P_i.

A framework for the multimodal supervoxel segmentation method is shown in Fig.6. Combining all MRI modalities helps supervoxel segmentation by enhancing weak image boundaries that appear in any single modality. For example, weak edges may appear in one image but present strong in other images from different imaging protocols. An example of this case is shown in Fig.7. The calculated supervoxel map using the multimodal segmentation method is overlaid on both FLAIR (top row of the first column in Fig.7) and p map (bottom row of the first column in Fig.7). The middle and the last columns in Fig.7 show two corresponding zoomed-in areas indicated in the FLAIR and p map images (yellow and orange rectangles). It is noted that, the middle column of the Fig.7 shows

strong edges in FLAIR image (shown by red ellipses), whereas corresponding edges in the *p* map are quite weak (shown by the blue ellipse). The opposite effect is apparent in the right column of Fig.7. By using the multimodal clustering method, the extracted supervoxel map provides good image boundaries even when boundaries are not clear in one image modality.

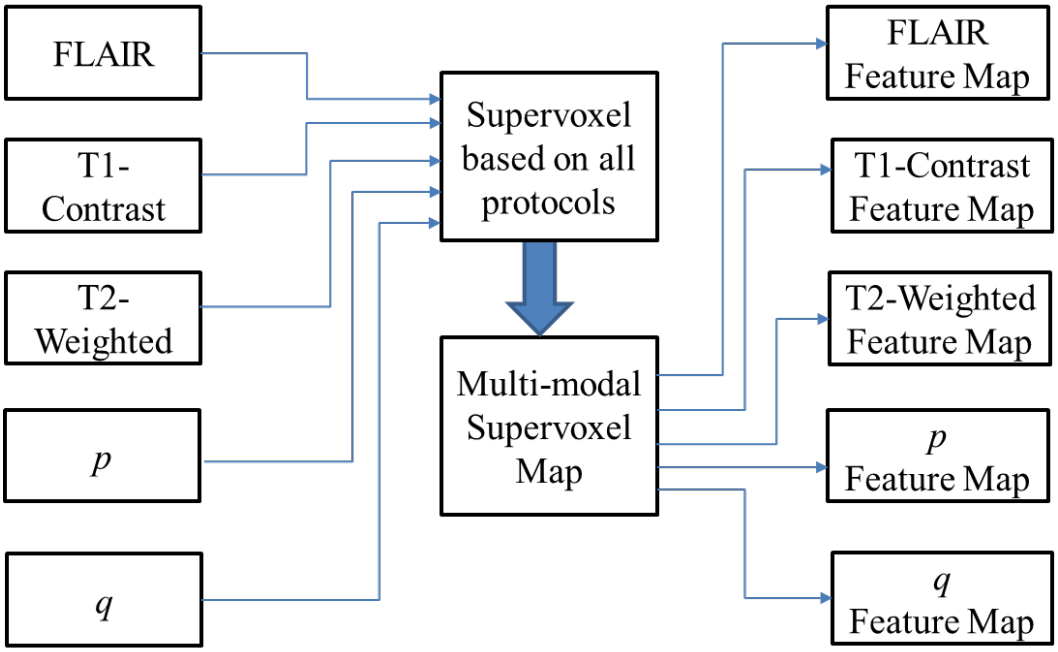

Fig. 6. Framework of multimodal supervoxel segmentation.

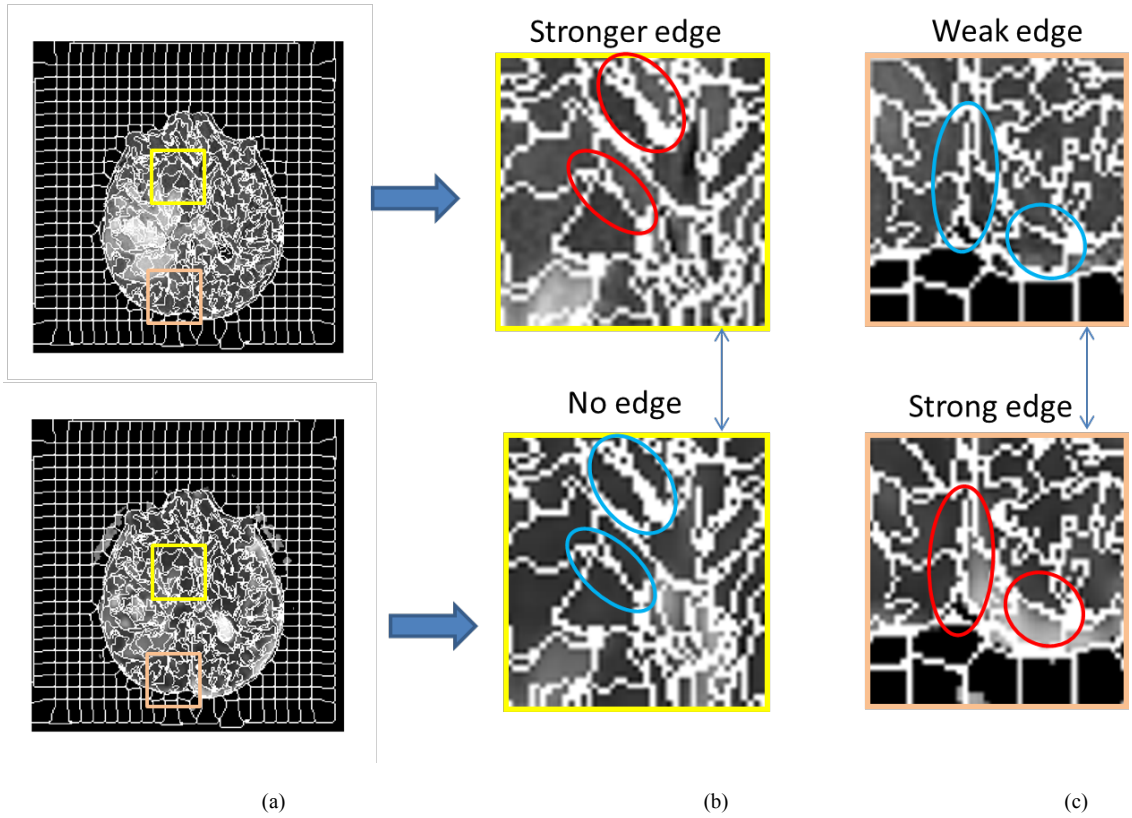

Fig. 7. An example of using a multimodal approach to improve supervoxel boundary by finding the edges which appear weak in one modality (blue ovals), but are apparent in the other modality (red ovals). (a) Upper image: FLAIR image overlaid by multimodal supervoxel segmentation, lower image: *p* map overlaid by the same multimodal supervoxel segmentation. (b) Zoomed-in area surrounded by the yellow box (in (a)) for both image modalities, (c) zoomed-in area surrounded by the red box (in (a)) for both image modalities.

Fig.8 shows a comparison of supervoxel segmentation of tumour core calculated from a single MRI modality (FLAIR) and from multimodal MRI (FLAIR, T1-weighted (with contrast), T2-weighted, *p* and *q* maps). As it can be seen in Fig.8, there are misalignments between supervoxels boundaries (computed from FLAIR) and the ground truth boundaries (see black ellipse in Fig.8(f)), whilst multimodal supervoxels show improvement in boundary alignment to the tumour core (see black ellipse in Fig.8 (i)).

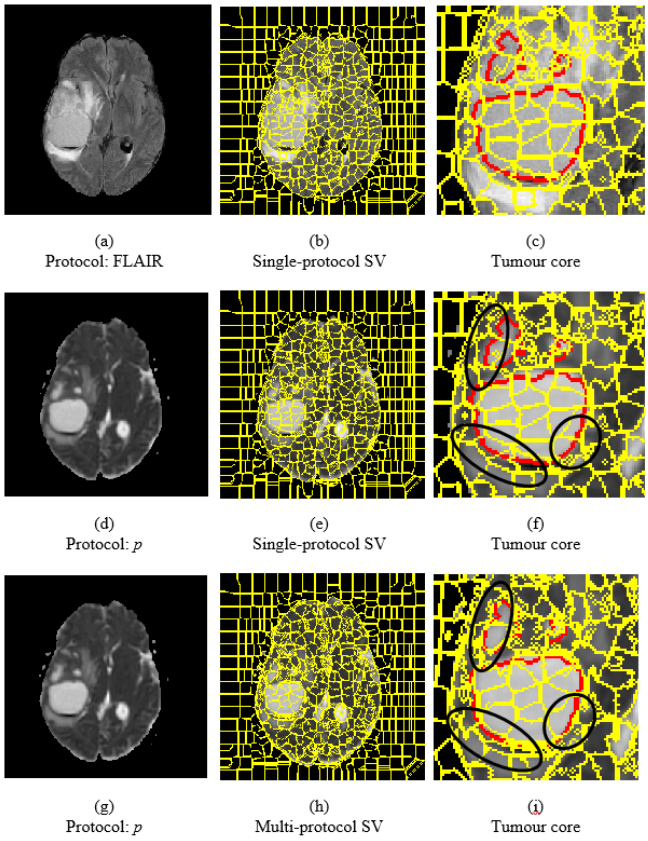

Fig. 8. One comparison example of tumour core supervoxel segmentation (SV) using single modality and multimodal MRI approaches. (a) FLAIR, (b): overlay of the corresponding supervoxels calculated using single modality (FLAIR), (c): zoomed-in of (b) on tumour area (to show the details of the SV boundaries) and overlay of tumour core (ground truth from manual delineation shown in red); (d): protocol *p* map, (e): Supervoxels calculated using single imaging modal (FLAIR) overlay on image protocol *p*, (f): zoomed-in of (e) on tumour area and overlay of tumour core (red). (g): protocol *p*, (h): Supervoxels calculated using multimodal (FLAIR, T1+contrast, T2, *p* and *q*) overlay on image protocol *p*. (i): zoomed-in of (h) on tumour area and overlay of tumour core (red). The boundaries surrounded by black ellipses in (f) and (i) highlighting the improvement of supervoxel boundary alignment with that of the tumour core using the proposed multimodal SV method. The supervoxels are initially sized 15 × 15 × 5 with $m = 0.2$ compactness.

2.5.Feature Extraction

Grouping the supervoxels for final segmentation of the tumour is based on the feature sets that are extracted from each supervoxel. In this section, first order statistical features and texton features are considered.

2.5.1. First Order Statistical Features

First order intensity statistics [38] are also referred to as voxel-intensity based features. First order statistical features express the distribution of grey levels within selected regions of interest (ROI), represented by supervoxels in our case. We use 16 features including the average, standard deviation, variance, mean of the absolute deviation, median absolute deviation, coefficient of variance, skewness, kurtosis, maximum, minimum, median and mode of the intensity values, central moments, range, interquartile range and entropy.

2.5.2. *Texton Features*

Due to the complexity and heterogeneity of tumour tissue, first order intensity features are generally not sufficient for an accurate segmentation. In this paper, texton features are considered to improve segmentation. Textons are small image elements that can be generated by convolution of the image with a set of image filters. We use the Gabor filter [31] defined in

$$G(x, y; \theta, \lambda, \psi, \sigma, \gamma) = \exp\left(-\frac{x'^2 + \gamma^2 y'^2}{2\,\sigma^2}\right)\exp\left(i\left(2\pi\frac{x'}{\lambda} + \psi\right)\right) \quad (7)$$

where, σ is the standard deviation of Gaussian envelope, γ is the spatial aspect ratio, λ is the wavelength of sinusoid and ψ is the phase shift. The terms x′ and y′ are calculated from the spatial orientation of the filter, θ, defined as

$$\begin{aligned} x' &= x\cos\theta + y\sin\theta \\ y' &= -x\sin\theta + y\cos\theta. \end{aligned} \tag{8}$$

The Gabor filter parameters were chosen empirically. Six different filter directions (θ) were considered: [0^o, 30^o, 45^o, 60^o, 90^o, 120^o] with filter sizes (σ) from 0.3 to 1.5 at steps of 0.3. The wavelengths of sinusoid coefficients of the Gabor filters (λ) were 0.8, 1.0, 1.2 and 1.5. This provided a filter bank of 120 filters.

Filter response images are the result of convolution of each filter with an MR image. For filters with the same size but different directions, the maximum response is considered, leading to a total of 20 filter responses (5 sizes, 4 wavelength coefficients). The texton map is then generated by applying 20-dimensional *k-Means* clustering to the 20 filter responses with a predefined number of clusters of $k_t = 5$ to represent tumour core, oedema and normal brain tissues. The normal brain tissues, i.e. white matter, grey matter, and cerebrospinal fluid (CSF), appear clearly with different textures and intensities in the images. Therefore, three clusters were assigned to the normal brain. However, they are considered as one object in the classification. To reduce computation time for clustering, the lowest number of clusters (i.e. $k_t = 5$) which are capable of separating tumour core and oedema from normal brain in the training set was chosen. Histograms of the texton parameter were then calculated for each supervoxel using the generated texton map. The distribution of the local

textures (descriptor) used to characterize the local object patterns, is one of the main features used in our tumour classification.

Table 1 summarises all extracted features. In total, there are 21 features for each MR image (protocol), so there are 105 features across the multimodal MRI data (FLAIR, T1-weighted (with contrast), T2-weighted, p and q maps). All feature calculations are performed on supervoxels and the extracted features for each MR image are concatenated to form the final multimodal feature vector.

Table 1. Number of features which are used for our learning based method.

Features calculated from each supervoxel	One Protocol	Multimodal (e.g. 5 protocols)
Statistical 1st order	16	80
Texton Histogram	5	25
Total	21	105

2.6. Random Forests Classification

Random forests (RF) is one of the best among classification algorithms [39]. It is an ensemble learning method that uses multiple decision trees. During the bagging process and at each attribute split, a random subset of features is used. After generating a large number of trees, a vote for the most popular class is made [40]. The structures of randomized trees are independent of training sample outputs.

In this study, all supervoxels within the brain are considered for classification. This represents a large amount of data, which is also unbalanced, as the number of supervoxels

related to normal brain is in the range of 6 to 30 times more than the number of tumour supervoxels (average ratio of 12:1). Therefore, the use of a robust classifier is essential to achieve accurate segmentation. Due to the many advantages of the RF classifier, (e.g. accuracy, efficiency in application to large datasets, and ability to handle unbalanced datasets) we use RF to classify each supervoxel into three tissue classes tumour core, oedema, and others.

The main parameters used in RF, i.e. the number of trees, the number of attributes, and tree depth, are chosen as follows: number of trees is 50 with depth of 15, and number of attributes (k_a) selected to perform the random splits for a specific number of features N_f is $k_a = \sqrt{N_f}$. For single modality and multimodal experiments, 5 and 10 attributes are selected, respectively. Further discussions are given in the Experimental Results Section (Section III-A)

In the training stage, the supervoxels are split into three classes: tumour core, oedema, and others. Supervoxels which have at least 50% overlap with tumour core, oedema regions or others (ground truth according to manual labelling) are labelled as the appropriate corresponding classes. The remaining supervoxels which do not meet this criterion, namely, do not represent a major class, are considered as unknown and excluded from the training phase. The RF classifier is trained based on these three labels. In the testing stage, the trained classifier is applied and labels are assigned to each supervoxel inside the brain. The tumour area is then obtained by grouping the supervoxels classified as either tumour core or the oedema class.

3. Experimental Results

Two datasets were analysed: (i) our clinical dataset described in Section II-A for training and validation of the algorithm, and (ii) the publicly available MICCAI BRATS 2013 dataset [24,25] for further comparison and assessment of the robustness of the method. For both datasets, quantitative evaluations (e.g. supervoxel classification accuracy and Dice score overlap measures for segmented objects vs ground truth) of the proposed method have been conducted using different imaging protocols (e.g. single modality or multimodal images).

For evaluation purpose, in order to make the evaluation consistent and comparable with BRATS evaluating protocols, the tumour core and oedema classes were merged to form the "whole tumour" class. In this case, tumour core and oedema were merged into one positive class (whole tumour) and the negative class was others. In the case of tumour core, the tumour core (positive class) was assessed against oedema and others (negative classes). In the case of oedema, the oedema (positive class) was assessed against tumour core and others (negative class).

The leave-one-out approach is used to train and test the model. Subsections 3.1 to 3.3 are focused on our clinical data cohort; whist subsection 3.4 evaluates results of our technique to the MICCAI BRATS 2013 dataset [5,24,25]. Subsection 3.5 presents statistical analysis on the two datasets.

3.1. Parameter Selection

For 2D superpixel calculation presented in our previous work [41], an optimal initial superpixel size of 5 was obtained. In the case of 3D supervoxels, the z direction is

determined based on Equation (2) from the slice thickness and image resolution. Due to the different resolutions used in our clinical data (all multimodal MRI data were co-registered to DTI with voxel dimensions 0.9375 mm × 0.9375 mm × 2.8 mm) and the BRATS dataset (isotropic voxel dimensions: 1 mm^3), the supervoxel initial sizes were chosen to be 8 × 8 × 3 for our clinical data, and 5 × 5 × 5 for the BRATS data. By visually inspecting the supervoxel boundaries and area, the value of $m = 0.05$ (in Equation (5)) was chosen, which presents coherent boundaries.

Implementation of the RF was performed in MATLAB 2016b based on the open source code provided in [42]. For the parameter selection, 8 patient cases were picked up randomly for training and 3 for validation. To select the optimum RF parameters, different ranges of number of trees and depth were assessed on our clinical data. 4-fold validation was used to select the optimal RF parameters (i.e. number of trees and depth). Each fold includes 3 patient cases for testing which were selected randomly without replacement, and remaining patient cases were considered as training (i.e. train/test ratio: 8/3). It should be noted that for 11 cases, the last fold includes 2 testing cases (i.e. train/test ratio: 9/2).

Classification accuracy was calculated for the testing fold in each iteration with different tree depth and number of trees. Values were averaged over all folds to determine the effects of number of trees and depth, and are presented in Fig.9. It can be seen in Fig.9 that, 50 trees with depth 15 give an optimum generalization and accuracy. These optimal parameters were also directly used in the analysis of the BRATS dataset (in Section D).

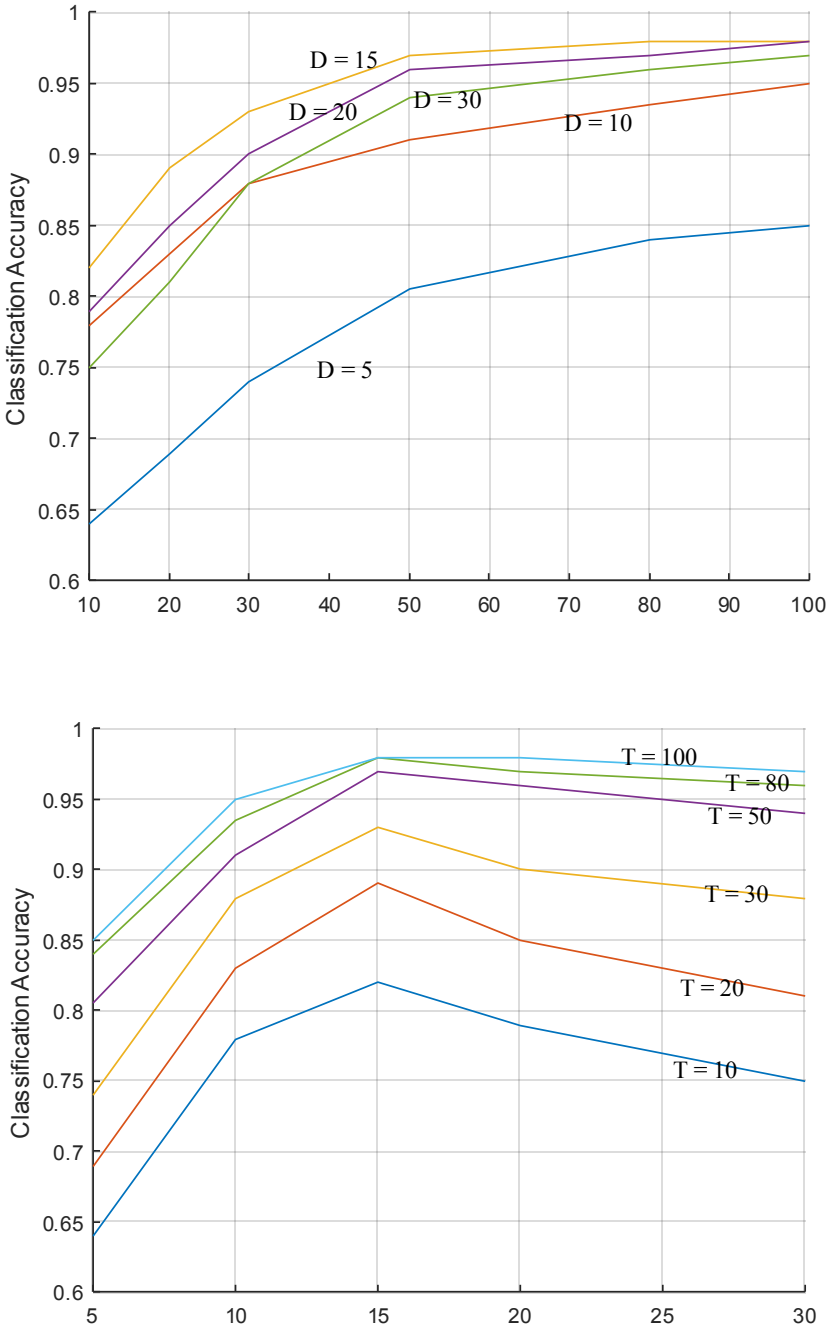

Fig. 9. Upper) Effect of number of trees on RF classification accuracy with different depths. Lower) effect of tree depth on RF classification accuracy with different numbers of trees.

Table 2 presents the proportion of features selected from each acquisition protocol using the RF from two experiments: conventional MRI data only (C-MRI, namely, FLAIR, T1-weighted (with contrast) and T2-weighted) and conventional MRI plus DTI (C-MRI+DTI). It can be seen that, for C-MRI, most of the features (61%) are selected from the FLAIR, which shows the importance of FLAIR for tumour segmentation. When DTI is added it has 24% of features selected from the DTI (i.e. p (16%) and q (8%) maps); the presence of DTI also slightly reduces the proportion of corresponding features from the C-MRI modalities alone. Our experimental results in the next section show that *p* and *q* maps improve the overall segmentation of tumour core.

Table 2. Ranking based on repetition in nodes of the forests of a RF with 50 number of trees and depth 15.

Experiment	FLAIR	T1C	T2	*p*	*q*
C-MRI	0.61	0.15	0.24	-	-
C-MRI+DTI	0.49	0.09	0.18	0.16	0.08

3.2. Supervoxel Classification Results

Regarding to the true class and estimated class labels, the following categories can be considered:

TP: Number of abnormal data classified correctly as abnormal.

TN: Number of normal data classified correctly as normal.

FP: Number of normal data classified incorrectly as abnormal.

FN: Number of abnormal data classified incorrectly as normal.

For the standard four classification measures (accuracy, precision, sensitivity,

specificity), both accuracy and specificity will give very high values due to the highly imbalanced nature of our data. Therefore, to properly evaluate the classification performance, only precision and sensitivity are considered. Consequently, in this paper, evaluation of the performance of the supervoxel classification method was performed using precision, sensitivity and balanced error rate (BER), which are calculated using

$$Precision = \frac{TP}{TP + FP}, \tag{9}$$

$$Sensitivity = \frac{TP}{TP + FN}, \tag{10}$$

$$BER = 1 - 0.5 \times \frac{\text{Sensitivity} + \text{Specificity}}{100}, \tag{11}$$

where

$$Specificity = \frac{TN}{TN + FP}. \tag{12}$$

To compare the supervoxel classification performances of our method using different MRI modalities for the whole tumour including core and oedema, three experiments are performed: 1) FLAIR only; 2) C-MRI data; 3) C-MRI+DTI.

In the first experiment, supervoxels are calculated based on FLAIR image only; whereas in the second and third experiments, supervoxels are calculated using Equation (5) based on different MRI modalities, i.e. C-MRI data in experiment 2 and C-MRI+DTI in experiment 3, respectively. The generated supervoxel map using different MRI protocols is then applied to each protocol image to extract features. As discussed in Section II-E and shown in Table 1, for each supervoxel, there are 21 features extracted from each protocol, so in

total 21 features for FLAIR only, 63 features for C-MRI data (e.g. FLAIR, T2 and T1-contrast), and 105 features for C-MRI+DTI (p and q maps). The random forests classification is then performed in each experiment to classify each supervoxel into normal brain tissue and tumour.

Table 3 shows the average results of supervoxel classification for the three experiments, using our clinical dataset. Results show significant improvement for classification of tumour core, oedema and the whole tumour using C-MRI+DTI, compared to use of the FLAIR image or the conventional MRI modalities alone.

Table 3. Classification results for supervoxels using single MRI modality (FLAIR).C-MRI (FLAIR, T1-C and T2) and C-MRI+DTI (C-MRI + p and q maps)

		Precision	Sensitivity	BER
Core	Single	69.49 ± 13.05	65.39 ± 8.38	0.18 ± 0.04
	C-MRI	73.64 ± 13.14	69.67 ± 7.59	0.15 ± 0.04
	C-MRI +DTI	83.44 ± 12.36	74.62 ± 18.95	0.13 ± 0.09
Oedema	Single	84.17 ± 7.93	79.28 ± 8.18	0.11 ± 0.04
	C-MRI	85.63 ± 8.24	80.59 ± 8.44	0.10 ± 0.04
	C-MRI +DTI	88.53 ± 7.37	84.57 ± 8.21	0.08 ± 0.04
Whole	Single	88.16 ± 6.38	81.88 ± 9.81	0.09 ± 0.05
	C-MRI	89.54 ± 6.18	83.66 ± 9.16	0.09 ± 0.05
	C-MRI +DTI	92.22 ± 5.80	86.25 ± 9.02	0.07 ± 0.05

3.3. Segmentation Results

The Dice score (DC) is used to evaluate the overlap ratio between the automated segmentation and the manual segmentation (gold standard):

$$\mathrm{DC} = \frac{2|M \cap S|}{|M|+|S|}, \tag{13}$$

where, M and S are the manual and proposed segmentation masks, respectively.

The DC ranges from 0 to 1 with closer to 1 representing better segmentation. Table 4 shows Dice scores comparing the ground truth with our automated method using the three experiment sets. Results show significant improvement in the segmentation of tumour core using the C-MRI+DTI approach with a DC of 0.78 compared to C-MRI (DC= 0.67) and the single FLAIR image (DC=0.54). This demonstrates that the multimodal approach by adding DTI increases the tumour segmentation accuracy.

Fig.10 shows examples of the segmentation of tumour core and oedema with three grade IV tumours using FLAIR only, C-MRI and C-MRI+DTI. It can be seen that several supervoxels are wrongly classified, e.g. false positive regions (FPs), in the segmented masks when using FLAIR and C-MRI images (see Fig.10 (c2) and (c3)) whereas adding DTI image modalities reduces these FPs, leading to a more accurate segmentation. For example, in Fig.10 (e1) and (e3), there are areas of tumour core which are missed by the C-MRI protocol, but these tumour areas can be detected by adding DTI modalities as shown in Fig.10 (d1) and (d3). This demonstrates an improvement in segmentation accuracy by the use of both C-MRI and DTI.

Table 4. Dice score comparison for the segmentation of tumour core, oedema and whole tumour using single protocol (FLAIR), C-MRI (FLAIR, T1-Contrast, T2-weighted) and C-MRI+DTI (FLAIR, T1-Contrast, T2-weighted, p and q).

No	FLAIR			FLAIR, T1-Contrast, T2-weighted			FLAIR, T1-Contrast, T2-weighted, p and q		
	Core	Oedema	Whole	Core	Oedema	Whole	Core	Oedema	Whole
1	0.79	0.63	0.75	0.84	0.69	0.77	0.91	0.71	0.79
2	0.55	0.66	0.70	0.60	0.69	0.72	0.84	0.73	0.77
3	0.63	0.70	0.71	0.68	0.70	0.74	0.76	0.71	0.73
4	0.65	0.73	0.78	0.76	0.77	0.82	0.85	0.86	0.91
5	0.56	0.81	0.82	0.62	0.83	0.83	0.68	0.85	0.85
6	0.65	0.72	0.75	0.72	0.73	0.76	0.83	0.81	0.85
7	0.53	0.85	0.86	0.74	0.86	0.87	0.86	0.85	0.86
8	0.42	0.85	0.85	0.58	0.86	0.86	0.62	0.87	0.87
9	0.34	0.82	0.83	0.59	0.83	0.85	0.70	0.89	0.91
10	0.41	0.86	0.86	0.68	0.85	0.86	0.83	0.86	0.88
11	0.34	0.83	0.84	0.52	0.85	0.87	0.67	0.86	0.87
Mean	0.54	0.77	0.79	0.67	0.79	0.81	0.78	0.82	0.84
STD	0.14	0.08	0.06	0.10	0.07	0.06	0.09	0.07	0.06

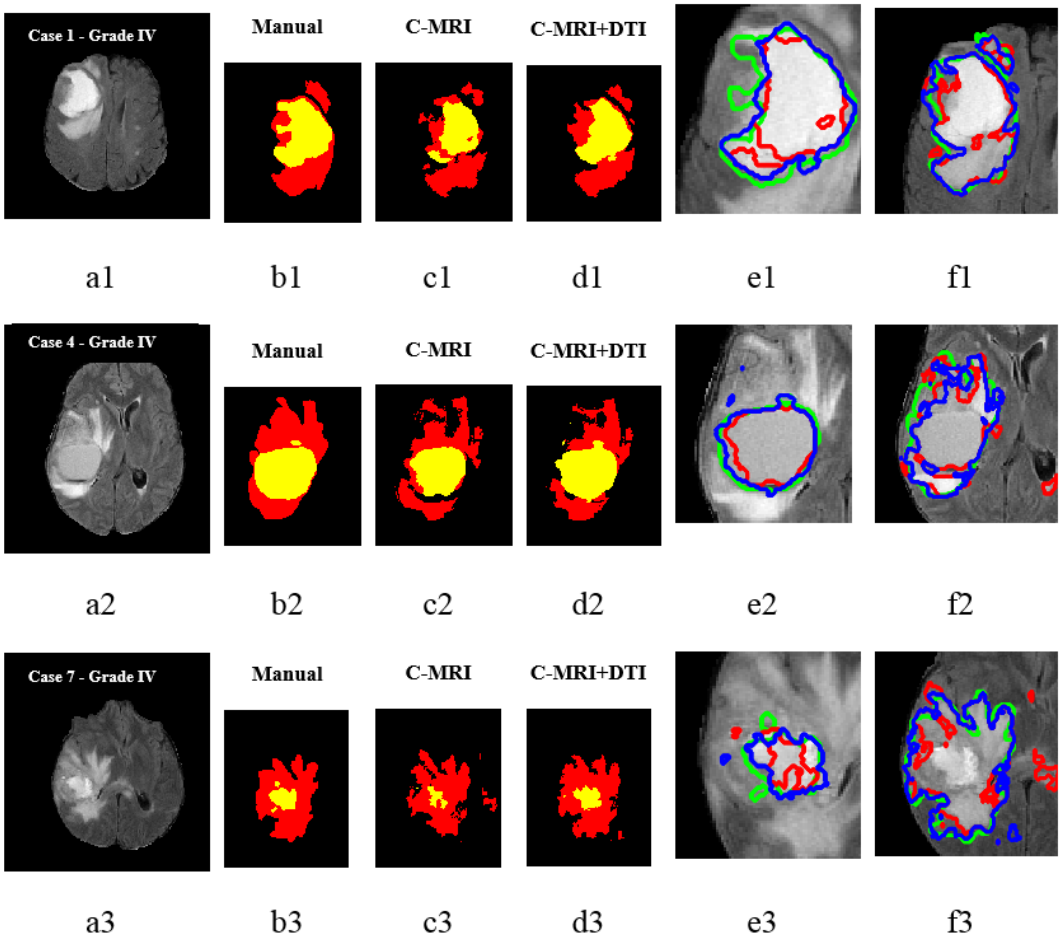

Fig. 10. Comparison examples of segmentation of tumour core and oedema using conventional MRI and conventional MRI plus DTI for three different cases with grade IV tumours. a) FLAIR image, b) manual segmentation of core (yellow region) and oedema (red region) c) segmentation using conventional MRI, d) segmentation using conventional MRI and DTI (M-MRI), e) comparison of both methods C-MRI (red), plus DTI (blue) and manual (green) segmentation for core (zoomed in), f) comparison of both methods C-MRI (red), plus DTI (blue) and manual (green) segmentation for oedema (zoomed in)

3.4. Evaluation on BRATS 2013 Dataset

To evaluate the robustness of our proposed method, it is also applied to the BRATS 2013

[24,25] patient dataset, which consists of 20 high grade and 10 low grade tumour types. In this dataset conventional FLAIR, T1-weighted, T2-weighted and T1-weighted with contrast image modalities are available. Data were acquired from different centres using different MR systems with field strengths of both 1.5T and 3T. The ground truth segmentations are manually provided by a human expert [5]. In this study, due to no DTI data available in the BRATS dataset, we evaluate the multimodal aspect of our proposed method, by calculating tumour segmentation performances using C-MRI (FLAIR, T1, T2 and T1+contrast), compared with that using the single imaging modality (FLAIR). The RF parameters were selected by 4-fold cross-validation experiment on our clinical dataset (discussed in section III-A) to assess robustness of RF parameter selection. RF was trained on BRATS dataset using 4-fold cross validation, similar to the clinical experiments. Two folds include 8 testing cases, and two folds with 7 testing cases, which were randomly selected without replacement. In each fold, the remaining patient cases were considered as training (i.e. train/test ratios were 22/8 and 23/7, respectively).

The parameters used for feature extraction are similar to those we used for our clinical datasets. This means that in terms of parameter selection, the clinical dataset was used as training/validation with the ratio: 8/3, and the test data were 30 BRATS patient cases. For the supervoxel segmentation the only parameter that is different from analysis of our own data is the initial superpixel size. This is due to the different voxel dimensions of the two datasets. The voxel dimension for all BRATS data is 1 mm × 1 mm × 1 mm. Therefore, the initial subvolumes are cubes with the same dimensions. The supervoxel size for segmenting both oedema and tumour core is defined as 5 mm × 5 mm × 5 mm considering small tumours in some images. Table 5 presents the average evaluation results using RF for

supervoxel classification of tumour core, oedema against the rest of tissues and also classification of whole tumour against the healthy tissue using single modality of FLAIR and multimodal approach on conventional MRI protocols (C-MRI) including FLAIR, T1-weighted, T1-weighted (with contrast) and T2-weighted imaging. Table 5 shows that the classification performances for different tumour regions (e.g. core, oedema, whole tumour) using C-MRI have been significantly improved compared to that using the single FLAIR imaging.

Table 6 shows the Dice score computed between ground truth segmentation and our automated segmentation using both FLAIR and C-MRI, on the 30 tumours of the BRATS dataset. This demonstrates that using a multimodal approach presents better overlap measures for tumour core, oedema, and whole tumour, compared to the use of FLAIR only.

Fig.11 shows comparison results of our automated method with the ground truth for both tumour core and oedema. Segmentation results are presented in axial slices overlaid on the FLAIR image (Fig.11 (e1), (e3), and (e3)). It can be seen that the segmentation from C-MRI results in better and more accurate tumour segmentation compared to the FLAIR imaging alone. For the tumour core segmentation, comparing Fig.11 (d2) (yellow) to Fig.11 (c2) (yellow), using a multimodal approach has achieved accurate segmentation compared to that using single modality. In particular, Fig.11 (c1) shows that several regions of normal brain are wrongly detected as tumour core and Fig.11 (c2) and (c3) show some regions of oedema that are wrongly classified as tumour core. However, those regions have been improved in Fig.11 (d1), (d2), and (d3) using C-MRI data.

The results of our proposed method on the BRATS 2013 dataset and the best scores in 2012 and 2013 challenges from other groups [5] are presented in Table 10. The method

proposed by Tustison *et al.* [12] was the winner of the on-site BRATS 2013 challenge. Our testing dataset is different with the dataset which was used in [12]. The labelling protocol in our method does not include enhancing tumour, therefore evaluation by the VSD online system blind test was not applicable. Since the ground truths for the training dataset were available, the corresponding labelling was used for evaluation of our method in which enhancing tumour and necrosis are merged together and formed one object class for tumour core. To fairly evaluate our proposed method, we also provide comparison with the best scores for analyses that used the clinical training dataset for evaluation their results. Reza et al [22] used the training clinical data to evaluate their method and obtained the best results for the same data as we used in this study. The average of the top 10 best results which used the same training dataset of BRATS 2013 according to their website [24] is also presented in Table 10. The comparison results in Table 10 demonstrate a good performance of our method for segmentation both of tumour core and whole tumour, with Dice scores of 0.80 and 0.89, respectively.

Table 5. Average classification results for superpixels from single modality (FLAIR) and multimodal C-MRI (FLAIR, T1, T1-Contrast and T2) of BRATS 2013 dataset (20 high grade and 10 low grade tumour)

		Precision	Sensitivity	BER
Core	Single modal	93.82 ± 5.08	90.69 ± 4.99	0.05 ± 0.02
	C-MRI	98.19 ± 1.90	94.75 ± 3.24	0.03 ± 0.02
Oedema	Single modal	94.01 ± 7.77	87.53 ± 5.91	0.06 ± 0.03
	C-MRI	98.31 ± 1.72	95.89 ± 4.49	0.02 ± 0.02
Whole	Single modal	98.25 ± 2.12	92.29 ± 4.68	0.04 ± 0.02
	C-MRI	99.46 ± 0.66	96.09 ± 3.00	0.02 ± 0.01

Table 6. Comparison results for Dice overlap between manual annotation and the automated segmentation using single modality (FLAIR) and multimodal C-MRI (FLAIR, T1, T1-Contrast and T2) of BRATS 2013.

		Core	Oedema	Whole
Single modality	Mean	0.65	0.79	0.85
	STD	0.09	0.09	0.06
C-MRI	Mean	0.80	0.89	0.89
	STD	0.09	0.05	0.04

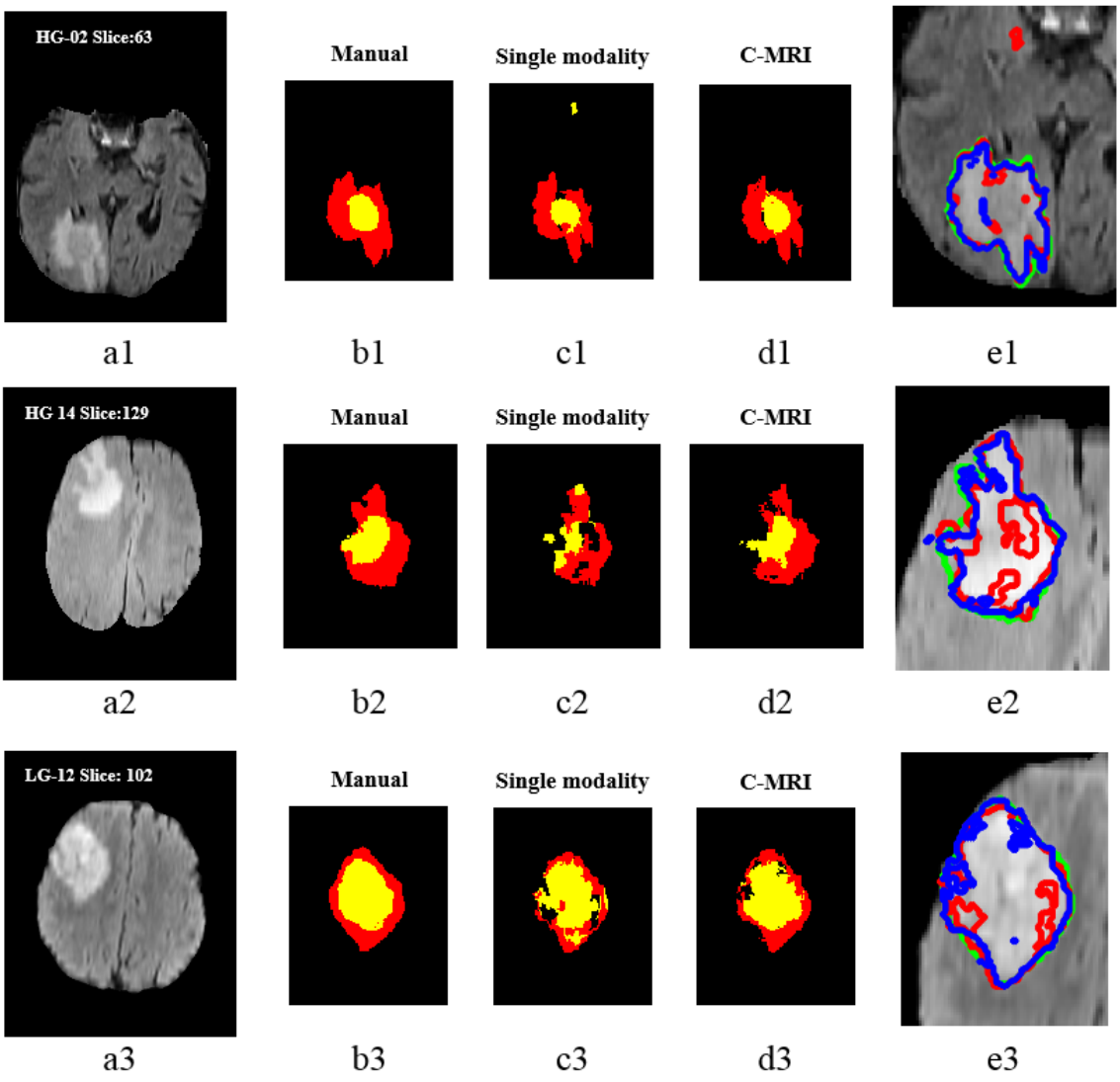

Fig. 11. Segmentation results overlay on the ground truth (whole tumour including oedema and core), using single (FLAIR) and multimodal (conventional MRI including FLAIR, T1, T1-contrast and T2), for three different cases with grade IV tumours; a) FLAIR image, b) manual segmentation of core (yellow region) and oedema (red region) c) segmentation using FLAIR d) segmentation using conventional MRI e) comparison of both methods: single modal (red), multimodal (blue) and manual (green) segmentation for whole tumour (zoomed in)

3.5. Statistical Analysis on the Two Datasets

The Wilcoxon signed-rank test was used on both our clinical dataset and the BRATS 2013 dataset to investigate if there were significant differences in both Dice scores and classification measures of precision, sensitivity and BER, from tumour segmentations obtained using the different imaging protocols, at a 95% confidence level.

Table 7 shows Wilcoxon signed-ranks test statistical results for whole tumour segmentation for the Dice scores and classification measures using the different imaging protocols on our clinical dataset (N=11). Results suggest that there is a statistically significant improvement in Dice scores and in classification measures of precision, sensitivity, BER, when using the C-MRI + DTI multimodal data compared to C-MRI or FLAIR alone.

Table 8 shows the corresponding Wilcoxon signed-ranks test statistical parameters for the BRATS 2013 dataset (N=30). These results also demonstrate a statistically significant improvement in Dice scores and all classification measures when using multimodal C-MRI data compared to FLAIR only. It is noted that there is no DTI available in the BRATS dataset.

Finally, we combined our results from the two different datasets (i.e. our clinical data and the BRATS data) in a single group containing either FLAIR or C-MRI (N=41). Table 9 shows the corresponding Wilcoxon signed-ranks test statistical results, which also indicate a statistically significant improvement in Dice scores and all classification measures when using the C-MRI protocol, instead of the FLAIR image alone.

Table 7. Wilcoxon signed-ranks test statistical parameters results for the segmentation overlap measure of Dice and the classification measures using different protocols (i.e. FLAIR only, conventional MRI (C-MRI), and conventional MRI plus DTI (C-MRI plus DTI), on our own dataset (11 subjects).

Whole Tumour	FLAIR *vs* C-MRI		FLAIR *vs* C-MRI + DTI		C-MRI *vs* C-MRI + DTI	
	p	z	p	z	p	z
DICE	0.003	-2.956	0.003	-2.952	0.003	-2.940
Precision	0.010	-2.578	0.004	-2.845	0.006	-2.756
Sensitivity	0.003	-2.936	0.003	-2.934	0.008	-2.667
BER	0.024	-2.264	0.007	-2.680	0.008	-2.666

Table 8. Wilcoxon signed-ranks test statistical parameters results for the segmentation overlap measure of Dice and the classification measures using different protocols (i.e. FLAIR only, and Conventional MRI (C-MRI), on BRATS dataset (30 subjects).

Whole Tumour	FLAIR *vs* C-MRI	
	p	z
DICE	< 0.001	-4.723
Precision	< 0.001	-4.021
Sensitivity	< 0.001	-4.762
BER	< 0.001	-4.051

Table 9. Wilcoxon signed-ranks test statistical parameters results for the segmentation overlap measure of Dice and the classification measures using different protocols (i.e. FLAIR only, and Conventional MRI (C-MRI), on both our own dataset and BRATS 2013 (41 subjects).

Whole Tumour	FLAIR *vs* C-MRI	
	p	z
DICE	< 0.001	-5.531
Precision	< 0.001	-4.743
Sensitivity	< 0.001	-5.566
BER	< 0.001	-4.589

4. Discussion

Our supervoxel calculation is based on SLIC [37] which was originally developed for natural images using 2D regular arrays without considering pixel resolutions. Whilst, our 3D clinical dataset is anisotropic, with different voxel resolutions along each dimension. To address this problem, we adapt the distance formulation in the supervoxel calculation from MR data with different acquisition parameters as shown in Equation (4). In this study, two different sets of data with different voxel dimension and slice thickness were used to evaluate our supervoxel method. Our clinical dataset has slice thickness three times more than the in-plane voxel resolutions. Therefore, the initial supervoxel is chosen to be rectangular shape (e.g. 8x8x3). Whilst, the BRATS dataset has been interpolated to 1mm isotropic resolution, so initial supervoxels are defined to be cubic. The supervoxel segmentation boundary for BRATS data has better resolution in the Z direction. This is the main reason why the segmentation results from BRATS data are in general better than that from our clinical data. The results in Table 4 and Table 6 confirm this and show the overall segmentation of tumour for our dataset has average of 0.84 with standard deviation of 0.06,

whereas for the BRATS dataset they are 0.89 and 0.04 respectively.

The reason for selecting RF as classifier was its advantages of handling large scale, high-dimensional and unbalanced dataset for multi object classification. A comparison of RF and SVM classifiers was conducted for superpixel-based [41] brain tumours segmentation, which suggested the more accuracy of RF compared to SVM.

The previous RF-based methods either optimise the RF for a voxel-wise classification [17–19] or improve the accuracy using a postprocessing stage such as conditional random fields [16]. The proposed method used patch-based classification which reduces the computational time.

An advantage of using supervoxel patches is its less computational time compared to the voxel-based classification algorithms, and all the image voxels can be included in the training phase. This is because the data points which form millions of voxels are now reduced to hundreds of thousands by using supervoxel patches. For instance, [16] and [19] used random points for training set, while we used all the supervoxels without any down-sampling.

The methods in [18] and [19] split the training set into HGG and LGG, while in our method all the tumour grades were mixed together and outperformed their methods without needing to separate the dataset based on the tumour grades, which emphasizes the fully automatic aspect of the method.

One limitation of supervoxel segmentation is that there is a minimum size for supervoxels regarding its parameters and image characteristics. For this reason, the method has a limitation in segmenting very small volumes. The overall Dice score for larger tumour cores is more than 80%; whereas for smaller tumour cores the overlap measure

decreases due to the initial supervoxel size. For example, the Dice scores for patient numbers 8 to 11 in Table 4 are relatively low. This is due to very small tumour cores for those data, which only contain a limited number of supervoxels.

Another limitation of supervoxel-based segmentation relates to the supervoxels at the tissue boundaries, which may include voxels from different tissues types. During the training phase, a threshold level of 50% was considered to label supervoxels. Although the supervoxel has the ability to track the boundaries of homogenous regions (as was explained in Fig.3 and depicted in Fig.7), there may be instances of complex structures which do not have the majority vote of a specific class. These supervoxels were considered to be uncertainty in object class and were excluded from the training phase. This is a limitation which may cause errors in boundaries of complex structures, which can be solved by further post-processing stages such as deformable models.

To evaluate the robustness and generality of our proposed supervoxel method, it was applied to the BRATS 2013 multimodal dataset. However, this dataset doesn't contain DTI protocols p and q. So, we only compare the single modal (FLAIR) against the multimodality (conventional) MRI. The supervoxel map generated from multimodality is different from single imaging modality based on FLAIR. The results show the improvement in segmentation of the tumour core. A zoomed-in image of the overlay of the tumour cores (shown in Fig.11) is depicted in Fig.12. To show the comparison between single modal and multimodal approaches, the segmentation results of both methods are overlaid on 2 different protocols, FLAIR and T1+C. As can be seen in Fig.12, the information from protocol T1+C improves the segmentation of tumour core, as the tumour core has more clear boundaries in this protocol. The homogenous region in the FLAIR

image (Fig.12 (a)) causes a wandering boundary (red dent in the figure) during single modality supervoxel segmentation, whereas using multimodal approach with the help of clear tumour core boundary in protocol T2 improves the segmentation accuracy (blue contour in Fig.12 (d)). The false positive region (shown in red in Fig.12 (b)) is the continuing of a supervoxel from adjacent slices. Using multimodal approach, the false positive regions can be successfully removed from the tumour core.

The proportion of the features selected from each protocol of the clinical dataset, using the RF shows that FLAIR presents the most important feature representation of 61% for the C-MRI only and 49% for C-MRI+DTI. The features extracted from the DTI protocols were found to be included as 24% of the total features (e.g. 16% from p map and 8% from q map). The experimental results show that combining the p and q protocols into the conventional MRI images improves the segmentation Dice score of core, oedema and whole tumour by 11%, 3% and 3%, respectively. Also, the classification performances of precision, sensitivity and BER have been improved for tumour core by 9.8%, 4.95%, 0.02, and for the whole tumour by 2.68%, 2.59% and 0.02, respectively.

The results of our proposed method on the BRATS 2013 clinical dataset were compared to the best scores in 2012 and 2013 challenges from other groups [5] shown in Table 10. The comparison results in Table 10 demonstrate a good performance of our method for segmentation both of tumour core and whole tumour, with Dice scores of 0.80 and 0.89, respectively.

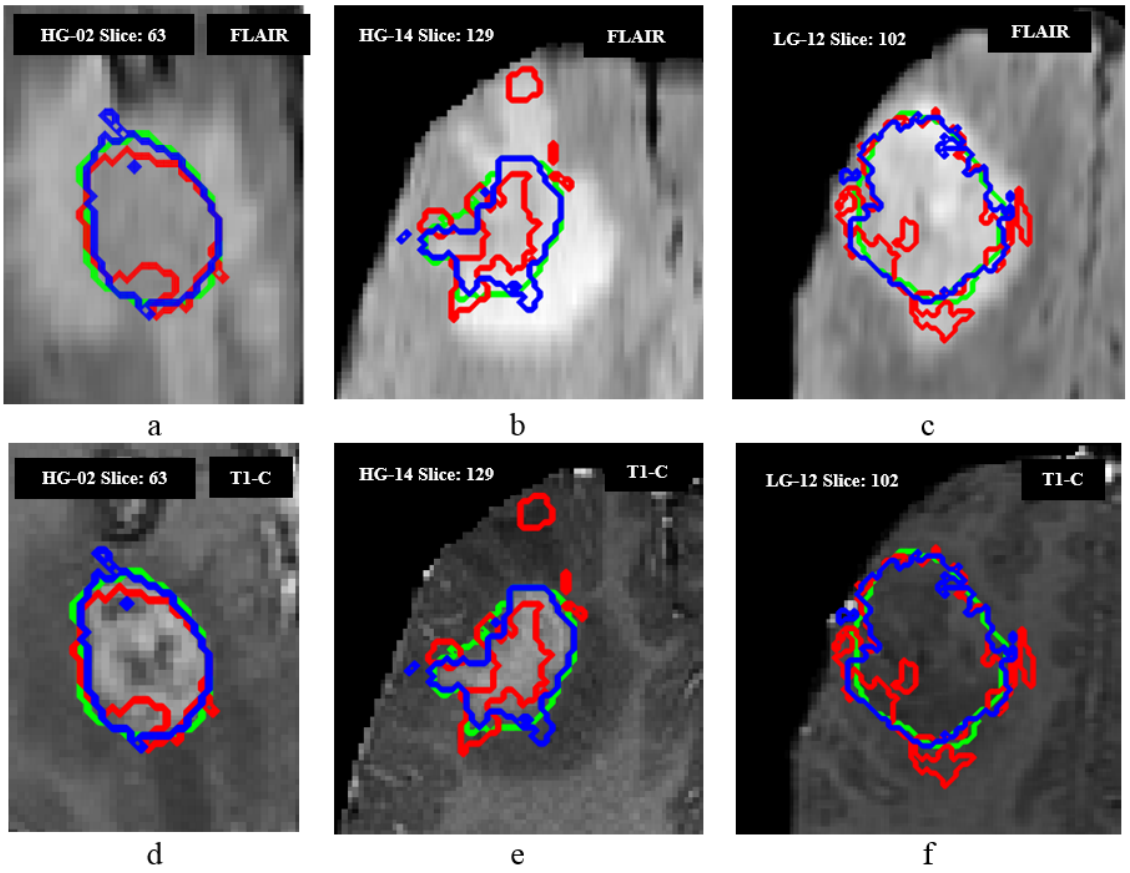

Fig. 12. Comparison between single modality and multimodal segmentation of core. a-c) FLAIR, d-f) T1-C.

Green: manual ground truth, red: single modal, blue: multimodal.

Table 10. Comparison with other methods which used BRATS 2013 dataset (MICCAI 2012 and 2013)

Work	Method	Toumor Core (Dice)	Whole (Dice)
Tutison [12]	RF and first order statistical features	0.78	0.87
Reza [18]	RF and texture features	0.91	0.92
Festa [18]	Local context features and RF	0.79	0.62
Bauer [16]	RF and CRF	0.68	0.48
Geremia [17]	Spatially adaptive RF	0.83	0.62
Lefkovits [19]	Optimised RF	0.70	0.82
Top 10 average	-	0.78	0.87
Our method	RF and multimodal supervoxel	0.80	0.89

5. Conclusion

A supervised learning based method is proposed for segmentation of tumour in multimodal MRI brain images. Supervoxels are calculated using information fusion from multimodal MRI images. A novel histogram of texton descriptors, calculated using a set of 3D Gabor filters with different sizes and orientations, are extracted on each supervoxel from different MRI imaging modalities. A random forests classifier is then used to classify each supervoxel into tumour (including tumour core and oedema) or normal brain tissue.

The method demonstrates promising results in the segmentation of brain tumour (core and oedema). Texton shows its advantages of providing significant information to distinguish various patterns in 3D spaces, and adding features from multimodal MRI images can largely increase the classification accuracy of the supervoxels in relation to manually defined gold standard. The experimental results using our clinical dataset demonstrate the further improvement of the segmentation and classification performance by combining the p- and q-map protocols from DTI modalities with the C-MRI, which can also be used for further segmentation of tissue subtypes; while the good performance achieved using the BRATS 2013 dataset shows robustness of the method. Our method provides a close match to expert delineation across all grades of glioma, leading to a faster and more reproducible method of brain tumour detection and delineation to aid patient management.

Our future work will be focused on using DTI modalities for more detailed segmentation of tumour tissue subtypes, such as necrosis and enhancing tumour.

Acknowledgements

This research was supported by European FP7 collaborative Project “MyHealthAvatar” (600929). MRI data were obtained during the EU FP7 “eTUMOUR” project (LSHC-CT-2004-503094).

References

[1] J.R. Fink, M. Muzi, M. Peck, K.A. Krohn, Continuing Education: Multi-modality Brain Tumor Imaging – MRI, PET, and PET/MRI, J Nucl Med. 56 (2015) 1554–1561. doi:10.2967/jnumed.113.131516.

[2] L.P. Clarke, R.P. Velthuizen, M.A. Camacho, J.J. Heine, M. Vaidyanathan, L.O. Hall, R.W. Thatcher, M.L. Silbiger, MRI segmentation: Methods and applications, Magnetic Resonance Imaging. 13 (1995) 343–368. doi:10.1016/0730-725X(94)00124-L.

[3] N. Gordillo, E. Montseny, P. Sobrevilla, State of the art survey on MRI brain tumor segmentation, Magn Reson Imaging. 31 (2013) 1426–1438. doi:10.1016/j.mri.2013.05.002.

[4] X. Xuan, Q. Liao, Statistical Structure Analysis in MRI Brain Tumor Segmentation, in: Fourth International Conference on Image and Graphics, 2007. ICIG 2007, 2007: pp. 421–426. doi:10.1109/ICIG.2007.181.

[5] B.H. Menze, A. Jakab, S. Bauer, J. Kalpathy-Cramer, K. Farahani, J. Kirby, Y. Burren, N. Porz, J. Slotboom, R. Wiest, L. Lanczi, E. Gerstner, M.A. Weber, T. Arbel, B.B. Avants, N. Ayache, P. Buendia, D.L. Collins, N. Cordier, J.J. Corso, A. Criminisi, T. Das, H. Delingette, Ç. Demiralp, C.R. Durst, M. Dojat, S. Doyle, J. Festa, F. Forbes, E. Geremia, B. Glocker, P. Golland, X. Guo, A. Hamamci, K.M. Iftekharuddin, R. Jena, N.M. John, E. Konukoglu, D. Lashkari, J.A. Mariz, R. Meier, S. Pereira, D. Precup, S.J. Price, T.R. Raviv, S.M.S. Reza, M. Ryan, D. Sarikaya, L. Schwartz, H.C. Shin, J. Shotton, C.A. Silva, N. Sousa, N.K. Subbanna, G. Szekely, T.J. Taylor, O.M. Thomas, N.J.

Tustison, G. Unal, F. Vasseur, M. Wintermark, D.H. Ye, L. Zhao, B. Zhao, D. Zikic, M. Prastawa, M. Reyes, K.V. Leemput, The Multimodal Brain Tumor Image Segmentation Benchmark (BRATS), IEEE Transactions on Medical Imaging. 34 (2015) 1993–2024. doi:10.1109/TMI.2014.2377694.

[6] S. Bauer, R. Wiest, L.-P. Nolte, M. Reyes, A survey of MRI-based medical image analysis for brain tumor studies, Phys Med Biol. 58 (2013) R97-129. doi:10.1088/0031-9155/58/13/R97.

[7] T. Haeck, F. Maes, P. Suetens, An untrained and unsupervised method for MRI brain tumor segmentation, in: 2016 IEEE 13th International Symposium on Biomedical Imaging (ISBI), 2016: pp. 265–268. doi:10.1109/ISBI.2016.7493260.

[8] M.T. El-Melegy, H.M. Mokhtar, Tumor segmentation in brain MRI using a fuzzy approach with class center priors, EURASIP Journal on Image and Video Processing. 2014 (2014) 21. doi:10.1186/1687-5281-2014-21.

[9] I. Njeh, L. Sallemi, I.B. Ayed, K. Chtourou, S. Lehericy, D. Galanaud, A.B. Hamida, 3D multimodal MRI brain glioma tumor and edema segmentation: A graph cut distribution matching approach, Computerized Medical Imaging and Graphics. 40 (2015) 108–119. doi:10.1016/j.compmedimag.2014.10.009.

[10] N. Sauwen, M. Acou, S. Van Cauter, D.M. Sima, J. Veraart, F. Maes, U. Himmelreich, E. Achten, S. Van Huffel, Comparison of unsupervised classification methods for brain tumor segmentation using multi-parametric MRI, NeuroImage: Clinical. 12 (2016) 753–764. doi:10.1016/j.nicl.2016.09.021.

[11] R. Helen, N. Kamaraj, CAD scheme to detect brain tumour in MR images using active contour models and tree classifiers, Journal of Electrical Engineering and Technology. 10 (2015) 670–675. doi:10.5370/JEET.2015.10.2.670.

[12] N.J. Tustison, K.L. Shrinidhi, M. Wintermark, C.R. Durst, B.M. Kandel, J.C. Gee, M.C. Grossman, B.B. Avants, Optimal Symmetric Multimodal Templates and Concatenated Random Forests for Supervised Brain Tumor Segmentation (Simplified) with ANTsR, Neuroinform. 13 (2014) 209–225. doi:10.1007/s12021-014-9245-2.

[13] A. Pinto, S. Pereira, H. Correia, J. Oliveira, D.M.L.D. Rasteiro, C.A. Silva, Brain Tumour Segmentation based on Extremely Randomized Forest with high-level features, in: 2015 37th Annual

International Conference of the IEEE Engineering in Medicine and Biology Society (EMBC), 2015: pp. 3037–3040. doi:10.1109/EMBC.2015.7319032.

[14] A. Chaddad, Automated feature extraction in brain tumor by magnetic resonance imaging using gaussian mixture models, International Journal of Biomedical Imaging. 2015 (2015). doi:10.1155/2015/868031.

[15] M. Goetz, C. Weber, F. Binczyk, J. Polanska, R. Tarnawski, B. Bobek-Billewicz, U. Koethe, J. Kleesiek, B. Stieltjes, K.H. Maier-Hein, DALSA: Domain Adaptation for Supervised Learning From Sparsely Annotated MR Images, IEEE Transactions on Medical Imaging. 35 (2016) 184–196. doi:10.1109/TMI.2015.2463078.

[16] S. Bauer, T. Fejes, J. Slotboom, R. Wiest, L.-P. Nolte, M. Reyes, Segmentation of brain tumor images based on integrated hierarchical classification and regularization, in: MICCAI BraTS Workshop. Nice: Miccai Society, 2012. http://www.istb.unibe.ch/unibe/portal/fak_medizin/ber_vkhum/inst_stb/content/e43946/e43949/e158631/e187931/pane187933/e187963/files187969/BauerBRATS2012_eng.pdf (accessed May 10, 2017).

[17] E. Geremia, B.H. Menze, N. Ayache, Spatially Adaptive Random Forests, in: 2013 IEEE 10th International Symposium on Biomedical Imaging, 2013: pp. 1344–1347. doi:10.1109/ISBI.2013.6556781.

[18] J. Festa, S. Pereira, J.A. Mariz, N. Sousa, C.A. Silva, Automatic brain tumor segmentation of multi-sequence mr images using random decision forests, in: Proceedings of NCI-MICCAI BRATS, 2013: pp. 23–26.

[19] L. Lefkovits, S. Lefkovits, L. Szilágyi, Brain Tumor Segmentation with Optimized Random Forest, in: Brainlesion: Glioma, Multiple Sclerosis, Stroke and Traumatic Brain Injuries, Springer, Cham, 2016: pp. 88–99. doi:10.1007/978-3-319-55524-9_9.

[20] N. Tustison, M. Wintermark, C. Durst, B. Avants, ANTs and Arboles, in: Proceedings of NCI-MICCAI BRATS, 2013: pp. 47–50.

[21] L. Zhao, D. Sarikaya, J.J. Corso, Automatic Brain Tumor Segmentation with MRF on Supervoxels, in: Proceedings of NCI-MICCAI BRATS, 2013: pp. 51–54.

[22] S. Reza, K.M. Iftekharuddin, Multi-class Abnormal Brain Tissue Segmentation Using Texture Features, in: Proceedings of NCI-MICCAI BRATS, 2013: pp. 38–42.

[23] D. Zikic, B. Glocker, E. Konukoglu, A. Criminisi, C. Demiralp, J. Shotton, O.M. Thomas, T. Das, R. Jena, S.J. Price, Decision Forests for Tissue-Specific Segmentation of High-Grade Gliomas in Multi-channel MR, in: N. Ayache, H. Delingette, P. Golland, K. Mori (Eds.), Medical Image Computing and Computer-Assisted Intervention – MICCAI 2012, Springer Berlin Heidelberg, 2012: pp. 369–376. doi:10.1007/978-3-642-33454-2_46.

[24] BRATS :: The Virtual Skeleton Database Project, (n.d.). https://www.smir.ch/BRATS/Start2012 (accessed July 3, 2016).

[25] M. Kistler, S. Bonaretti, M. Pfahrer, R. Niklaus, P. Büchler, The virtual skeleton database: an open access repository for biomedical research and collaboration, J. Med. Internet Res. 15 (2013) e245. doi:10.2196/jmir.2930.

[26] A. Crimi, B. Menze, O. Maier, M. Reyes, H. Handels, eds., Brainlesion: Glioma, Multiple Sclerosis, Stroke and Traumatic Brain Injuries, Springer International Publishing, Cham, 2016. http://link.springer.com/10.1007/978-3-319-30858-6 (accessed July 17, 2016).

[27] R. Verma, E.I. Zacharaki, Y. Ou, H. Cai, S. Chawla, S.-K. Lee, E.R. Melhem, R. Wolf, C. Davatzikos, Multiparametric Tissue Characterization of Brain Neoplasms and Their Recurrence Using Pattern Classification of MR Images, Academic Radiology. 15 (2008) 966–977. doi:10.1016/j.acra.2008.01.029.

[28] A.F. Kazerooni, M. Mohseni, S. Rezaei, G. Bakhshandehpour, H.S. Rad, Multi-parametric (ADC/PWI/T2-w) image fusion approach for accurate semi-automatic segmentation of tumorous regions in glioblastoma multiforme, Magn Reson Mater Phy. 28 (2015) 13–22. doi:10.1007/s10334-014-0442-7.

[29] A.Y.C.C. Wei Wu, Brain tumor detection and segmentation in a CRF (conditional random fields) framework with pixel-pairwise affinity and superpixel-level features, International Journal of Computer Assisted Radiology and Surgery. 9 (2013). doi:10.1007/s11548-013-0922-7.

[30] A. Peña, H. a. L. Green, T.A. Carpenter, S.J. Price, J.D. Pickard, J.H. Gillard, Enhanced visualization and quantification of magnetic resonance diffusion tensor imaging using the p:q tensor decomposition, Br J Radiol. 79 (2006) 101–109. doi:10.1259/bjr/24908512.

[31] W. Wu, A.Y.C. Chen, L. Zhao, J.J. Corso, Brain tumor detection and segmentation in a CRF (conditional random fields) framework with pixel-pairwise affinity and superpixel-level features, Int J Comput Assist Radiol Surg. 9 (2014) 241–253. doi:10.1007/s11548-013-0922-7.

[32] T. Jones, B. Bell, T. Barrick, A novel whole-brain DTI segmentation technique for brain tumour delineation and diagnosis, in: Proceedings of the International Society for Magnetic Resonance in Medicine (ISMRM), 2012: p. 188.

[33] T.R. Barrick, C.A. Clark, Singularities in diffusion tensor fields and their relevance in white matter fiber tractography, NeuroImage. 22 (2004) 481–491. doi:10.1016/j.neuroimage.2004.02.001.

[34] FSL, (n.d.). https://fsl.fmrib.ox.ac.uk/fsl/fslwiki (accessed February 28, 2017).

[35] SPM - Statistical Parametric Mapping, (n.d.). http://www.fil.ion.ucl.ac.uk/spm/ (accessed February 28, 2017).

[36] L.G. Nyúl, J.K. Udupa, X. Zhang, New variants of a method of MRI scale standardization, IEEE Trans Med Imaging. 19 (2000) 143–150. doi:10.1109/42.836373.

[37] R. Achanta, A. Shaji, K. Smith, A. Lucchi, P. Fua, S. Süsstrunk, SLIC Superpixels Compared to State-of-the-Art Superpixel Methods, IEEE Transactions on Pattern Analysis and Machine Intelligence. 34 (2012) 2274–2282. doi:10.1109/TPAMI.2012.120.

[38] A.K. Jain, Fundamentals of Digital Image Processing, 1 edition, Prentice Hall, Englewood Cliffs, NJ, 1988.

[39] A. Liaw, M. Wiener, Classification and regression by randomForest, 2 (2002) 18–22.

[40] L. Breiman, Random Forests, Machine Learning. 45 (2001) 5–32. doi:10.1023/A:1010933404324.

[41] M. Soltaninejad, G. Yang, T. Lambrou, N. Allinson, T.L. Jones, T.R. Barrick, F.A. Howe, X. Ye, Automated brain tumour detection and segmentation using superpixel-based extremely randomized trees in FLAIR MRI, Int J CARS. (2016) 1–21. doi:10.1007/s11548-016-1483-3.

[42] R. Taormina, MATLAB_ExtraTrees - File Exchange - MATLAB Central, (n.d.). http://uk.mathworks.com/matlabcentral/fileexchange/47372-rtaormina-matlab-extratrees (accessed February 16, 2016).

[43] M. Havaei, A. Davy, D. Warde-Farley, A. Biard, A. Courville, Y. Bengio, C. Pal, P. M. Jodoin, H. Larochelle, Brain tumor segmentation with Deep Neural Networks, Medical Image Analysis. 35 (2017) 18-31. dx.doi.org/10.1016/j.media.2016.05.004

[44] K. Kamnitsas, C. Ledig, V.F.J. Newcombe, J.P. Simpson, A.D. Kane, D.K. Menon, D. Rueckert, B. Glocker, Efficient multi-scale 3D CNN with fully connected CRF for accurate brain lesion segmentation, Medical Image Analysis. 36 (2017) 61–78. doi:10.1016/j.media.2016.10.004.

[45] X. Zhao, Y. Wu, G. Song, Z. Li, Y. Zhang, Y. Fan, A deep learning model integrating FCNNs and CRFs for brain tumor segmentation, Medical Image Analysis. 43 (2018) 98-111. doi.org/10.1016/j.media.2017.10.002